Draft version March 11, 2016
Preprint typeset using LaTeX style emulateapj v. 04/17/13

arXiv:1603.03121v1 [astro-ph.SR] 10 Mar 2016

OBSERVATION OF A QUASI-PERIODIC PULSATION IN HARD X-RAY, RADIO AND EXTREME-ULTRAVIOLET WAVELENGTHS

PANKAJ KUMAR[1], VALERY M. NAKARIAKOV[2,3,4], KYUNG-SUK CHO[1]
[1]Korea Astronomy and Space Science Institute (KASI), Daejeon, 305-348, Republic of Korea
[2]Centre for Fusion, Space and Astrophysics, Department of Physics, University of Warwick, CV4 7AL, UK
[3]School of Space Research, Kyung Hee University, Yongin, 446-701, Gyeonggi, Republic of Korea and
[4] Central Astronomical Observatory at Pulkovo of RAS, 196140 St Petersburg, Russia
Draft version March 11, 2016

ABSTRACT

We present multi-wavelength analysis of a quasi-periodic pulsation (QPP) observed in the hard X-ray, radio, and extreme-ultraviolet (EUV) channels during an M1.9 flare occurred on 23–24 September 2011. The non-thermal hard X-ray emission in 25-50 keV observed by RHESSI shows five distinct impulsive peaks of decaying amplitude with a period of about three minutes. Similar QPP was observed in the microwave emission recorded by the Nobeyama Radioheliograph and Polarimeter in the 8.8, 15, 17 GHz channels. Interestingly, the 3-min QPP was also observed in the metric and decimetric radio frequencies (25–180, 245, 610 MHz) as repetitive type III bursts. Multi-wavelength observations from the SDO/AIA, Hinode/SOT, and STEREO/SECCHI suggest a fan-spine topology at the eruption site, associated with the formation of a quasi-circular ribbon during the flare. A small filament was observed below the fan-loops before the flare onset. The filament rose slowly and interacted with the ambient field. This behaviour was followed by an untwisting motion of the filament. Two different structures of the filament showed ∼3-min periodic alternate rotation in the clockwise and counterclockwise directions. The 3-min QPP was found to highly correlate with 3-min oscillations in a nearby sunspot. We suggest that the periodic reconnection (modulated either by sunspot slow-mode wave or by untwisting filament) at a magnetic null-point most likely causes the repetitive particle acceleration, generating the QPP observed in hard X-ray, microwave and type III radio bursts.
Subject headings: Solar flare – coronal loops, magnetic field, sunspots, magnetic reconnection

1. INTRODUCTION

Quasi-periodic pulsations (QPPs) with periods from a few seconds to several minutes are often observed during solar flares in X-ray, radio, and optical wavelength bands (e.g. Aschwanden 2004; Nakariakov & Melnikov 2009; Nakariakov et al. 2010). Similar QPP have also been detected in stellar flares (e.g. Mathioudakis et al. 2003; Pandey & Srivastava 2009; Anfinogentov et al. 2013; Balona et al. 2015; Pugh et al. 2015). The study of the QPP phenomenon is promising in the context of understanding the basic physics of flaring energy releases, charged particle acceleration, and for the indirect estimation of plasma parameters by the method of magnetohydrodynamic (MHD) seismology (e.g. Roberts 2000; De Moortel & Nakariakov 2012; Liu & Ofman 2014).

Production of QPPs in flares may be associated with several physical mechanisms associated with flares. The following mechanisms could be responsible for the QPP formation:

(i) QPP may be associated with a periodic, bursty regime of spontaneous magnetic reconnection, e.g. by tearing of the current sheet associated with the formation of multiple plasmoids (Kliem et al. 2000). The coalescence and interaction of different plasmoids moving up and down along the flaring current sheet can periodically modulate the bidirectional (up and down) acceleration of electrons (Bárta et al. 2007, 2008). In this case, drifting pulsating structures (DPSs) in the decimetric radio frequencies are expected to be observed (Karlický et al. 2010). Recently, multiple plasmoids moving bidirectionally along an apparent current sheet have been observed in EUV (Takasao et al. 2012). Simultaneous observations of multiple plasmoids and drifting pulsating structures (for a duration of ∼1 min) have been recently reported by Kumar & Cho (2013). Therefore, tearing of the current sheet and formation of multiple plasmoids can generate QPPs in radio and hard X-ray with periods from seconds to several minutes.

(ii) Coalescence of current-carrying coronal loops can result in periodic variation of the coalescence current sheet width, accompanied by periodic production of non-thermal electrons. It would generate QPPs in hard X-ray and radio bands (Tajima et al. 1987; Kumar et al. 2010). In particular, the 25–48-s QPPs detected in the rising phase of solar flares were associated with this mechanism by Fárník et al. (2003).

(iii) In the model recently proposed by Takasao et al. (2015) numerical simulations of the shock formation and evolution of the thermal structure in and above post-flare loops demonstrated that the strength of the termination shock shows a quasi-periodic oscillation. This scenario can also be classified spontaneously-generated QPP.

(iv) The interaction of MHD waves (e.g., fast-mode wave, slow-mode wave or torsional Alfvén waves) with the reconnection site may lead to induced QPPs. Ning et al. (2004) studied recurrent explosive events with a period of ∼3–5 min, and suggested that their triggering could be caused by an MHD wave. A fast-mode MHD

pankaj@kasi.re.kr

wave model proposed by Nakariakov et al. (2006) links triggering of QPP with a transverse oscillation of a coronal loop situated near the reconnection region/current sheet. Doyle et al. (2006) studied the repetitive occurrence of explosive events at a coronal hole boundary, and suggested the periodic triggering of reconnection by a kink oscillation of the flux tubes in the closed field line region. Chen & Priest (2006) modelled explosive events in the transition region, and showed that the repetitive reconnection (e.g., with the period of 3–5 min) could be triggered by a slow-mode MHD wave. This idea was further developed by Sych et al. (2009) who demonstrated that 3-min QPP observed during a flare could be triggered by the along-the-field leakage of 3-min slow-mode oscillations in the umbra of a nearby sunspot. In two-ribbon flares, repetitive reflection of flare-excited slow-mode waves from footpoints of the flaring arcade may also be a possible mechanism for triggering the periodic reconnection (Nakariakov & Zimovets 2011). In that scenario, the hard X-ray source moves with a subsonic and sub-Alfvénic speed along the neutral line, which is consistent with observations.

Despite significant progress in both the theoretical modelling and observational detection, the specific mechanisms for QPP observed in solar and stellar flares are still not well understood and need further investigations. In particular, analysis of QPPs in high-resolution multi-wavelength observations (e.g., simultaneously in EUV, X-rays and radio) can provide a more complete picture of the flare event, and allow us to draw important conclusions on the QPP generation mechanisms.

Recently, Kumar et al. (2015) studied a decaying QPP with the period about 202 s in the 6–12 keV X-ray and EUV channels. They found that the QPP was generated by periodic reconnection caused by an untwisting small filament at a 3D null point in a fan-spine magnetic topology. Energetic particles accelerated along the arcade loops toward the opposite footpoints and precipitated there, were associated with periodic EUV brightening. Apart from the 202-s QPP, a 409-s oscillation was also observed as a periodic alternate flow along the arcade loops, and interpreted as a slow-mode (longitudinal) wave excited by a flare triggered at one of the footpoints of the arcade loops.

In this paper, we analyse a QPP observed in hard X-rays (25–50 keV), microwaves (17 GHz), and EUV emission in an M1.9 flare on 23–24 September 2011. The flare exhibits a quasi-circular ribbon, which suggests the possible magnetic configuration to be a fan-spine topology at the boundary of the active region NOAA 11302. In Section 2, we present the observations and results. In the last section, we summarize and discuss our results.

2. OBSERVATIONS AND RESULTS

The *Atmospheric Image Assembly* (AIA; Lemen et al. 2012) onboard the *Solar Dynamics Observatory* (SDO; Pesnell et al. 2012) captures full disk images of the Sun in the field-of-view of about 1.3 $R_\odot$, the spatial resolution of 1.5″ (0.6″ pixel^{-1}) and the time cadence of 12 s, in ten extreme ultraviolet (EUV) and UV channels. The present study utilizes 171 Å (Fe IX, corresponding to the temperature T of about 0.7 MK), 94 Å (Fe XVIII, $T \approx 6.3$ MK), 131 Å (Fe VIII, Fe XXI, Fe XXIII, i.e., $T \approx 0.4$, 10 and 16 MK, respectively), 304 Å (He II, $T \approx 0.05$ MK), and 1,600 Å (C IV + continuum, $T \approx 0.1$ MK and 5000 K) images. We also used Heliospheric and Magnetic Imager (HMI) magnetograms (Schou et al. 2012) to investigate the magnetic configuration of the active region. We used RHESSI (Lin et al. 2002) hard X-ray (HXR) and Nobeyama Radioheliograph (NoRH; Nakajima et al. 1994) and Polarimeter (NoRP; Nakajima et al. 1985) observations to determine the HXR and microwave source location of the observed QPP.

The active region (AR) NOAA 11302 was located near the eastern limb (N12E56) on 23 September 2011, with a $\beta\gamma$ magnetic configuration. The QPP reported here, was observed during an M1.9 flare. The flare was triggered at the edge of the AR, where the fan-shaped loops were observed within the pre-existing active region. The flare started at ∼23:48 UT, peaked at ∼23:56 UT, and ended at ∼00:04 UT.

2.1. *Quasi-periodic pulsation*

Figure 1(a) displays the GOES soft X-ray flux profile (3-s cadence) in 1–8 Å channel and its derivative (red curve) estimated by using the 3-point Lagrangian interpolation method. Interestingly, the time derivative of the flux profile reveals a clear QPP. Fig. 1(b) shows RHESSI hard X-ray count rate time profiles (4-s cadence) in the 12–25 keV (black), 25–50 keV (blue), and 50–100 (red) keV channels. The decaying oscillation is especially very clear in the 25–50 keV channel. Five distinct bursts of the energy release are marked by 1 to 5. The 50–100 keV flux profile shows only first two bursts of the energy release, while the other three bursts are not detected in this energy range. To investigate the QPP in radio channels, we plotted Nobeyama Radio Polarimeter (NoRP, 1-s cadence) flux profiles in 2, 3.75, 9.4, and 17 GHz channels (Fig. 1(c)). We can see a clear QPP cotemporal with the RHESSI HXR bursts.

Fig. 1(d) displays the dynamic radio spectrum in 25–180 MHz frequency observed at the Learmonth radio observatory, Australia. We can see a series of quasi-periodic type III radio bursts during the flare. We also used Radio Solar Telescope Network (RSTN) 1-s cadence data from the Learmonth observatory to see the radio flux density profiles in 245, 610, 8,800, and 15,400 MHz frequency bands (Fig. 1(d-h)). QPP is clear in all the light curves not only in the high frequency radio bursts (2, 9.4, 17 GHz) but also in the low frequency (245, 610 MHz) channels.

Nonthermal electrons responsible for the HXR and microwave emissions may be accelerated by the same process during the flare, e.g. magnetic reconnection (Kundu 1961, 1965), but have different energies (Kai 1986). The foot-point HXR emission is generated during the precipitation of the nonthermal electrons with the energies of tens of keV, whereas the microwave emission is produced by trapped nonthermal electrons of several hundreds of keV (Kundu et al. 1994; White et al. 2003; Asai et al. 2013). Spatially, the microwave emission comes from the body of the flaring loop, while the HXR emission comes from its footpoints and loop-top. Therefore, microwave and HXR emissions are generated by the nonthermal electrons accelerated in the reconnection site and pre-

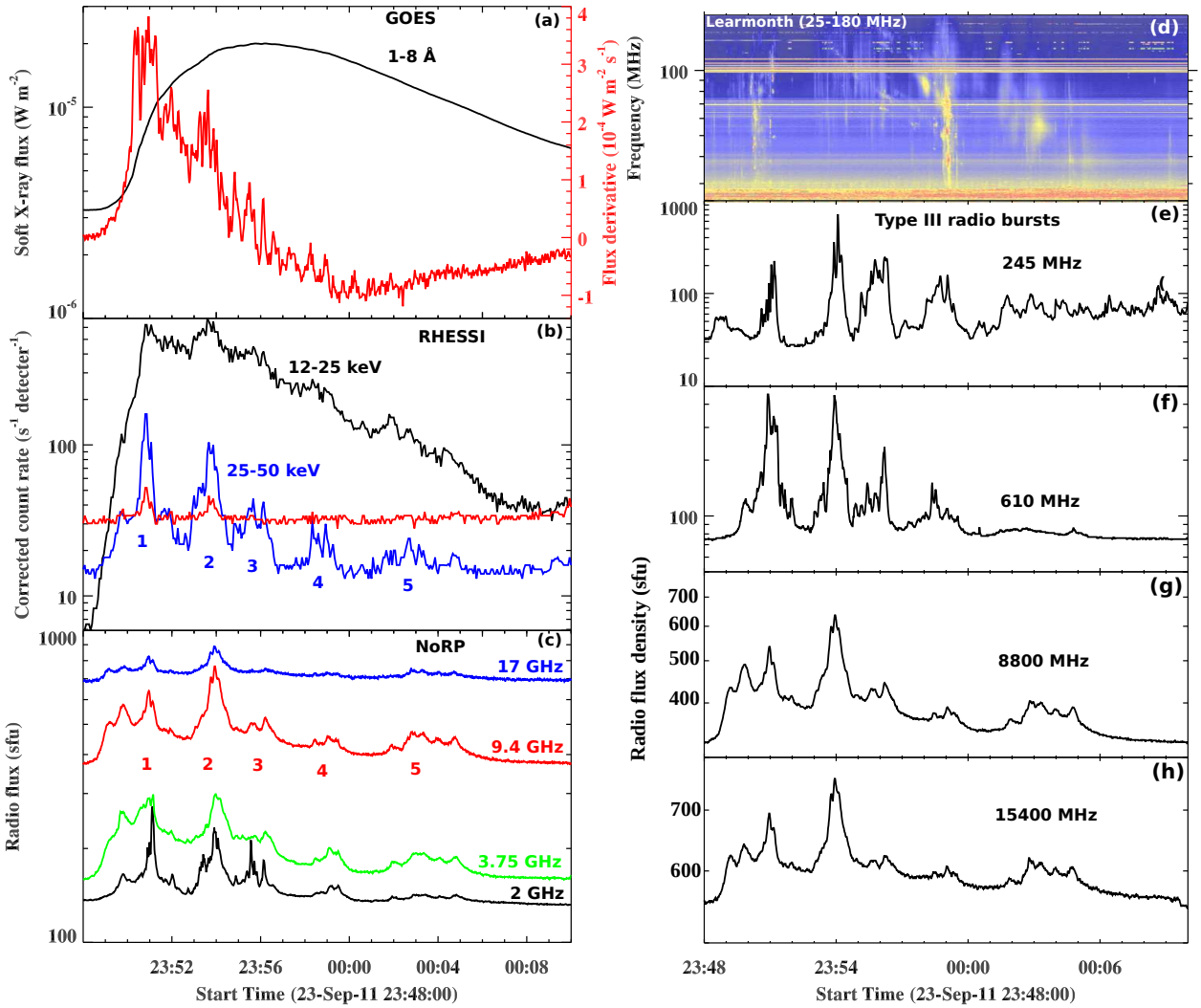

FIG. 1.— (a) GOES soft X-ray flux profile in the 1–8 Å channel and its time derivative (red). (b) RHESSI hard X-ray flux profiles in 12–25, 25–50, and 50–100 keV channels. (c) NoRP flux profiles in 2, 3.75, 9.4, and 17 GHz frequency bands. (d) Learmonth dynamic radio spectrum in 25–18 MHz frequency, showing bunches of type III radio bursts. (e-h) RSTN radio flux density profiles in 245, 610, 8,800, 15,400 MHz frequencies from the Learmonth solar observatory.

cipitated/transported downward into the chromosphere. In contrast, the 25–180 and 245 MHz channels show quasi-periodic type III radio bursts excited by the non-thermal electrons propagating upward (along the open field lines) from the reconnection site to the interplanetary medium. The emission at the decimetric frequency (e.g. 610 MHz) is generally associated with the acceleration region (Aschwanden & Benz 1997; Aschwanden 2004). Type III radio bursts above 1 GHz are generated by the electron beams propagating downward from the acceleration site (Bastian et al. 1998). Since we observed ∼3-min periodicity in type III radio bursts (below 300 MHz), microwave bursts (above 1 GHz), and HXR bursts (25-50 keV) simultaneously, therefore, it indicates the bi-directional acceleration/injection of electrons (Aschwanden & Benz 1997) from the acceleration region. Thus, this event suggests the quasi-periodic acceleration of electrons, that then propagate from the reconnection site upwards and downwards, bidirectionally.

Although the oscillatory pattern is clear in all the original light curves, we used the Lomb–Scargle periodogram method (e.g. Scargle 1982; Horne & Baliunas 1986) for the determination of the oscillation period and its confidence level. Figure 2(a,b) shows the results of the periodogram analysis (i.e., the power spectra) for the 25–50 keV RHESSI hard X-ray signal (4-s cadence) and RSTN 15.4 GHz radio signal (1-s cadence). The confidence level of 99% is marked by the horizontal dashed line. A period of approximately 3 min (above 99% confidence level) is revealed in both the RHESSI and microwave signals. We would like to stress that the confidence levels shown in the power spectra correspond to the highest spectral peaks only, and cannot be used for the determination of the significance of the secondary peaks. We also applied Morlet wavelet analysis (Torrence & Compo 1998) on the RHESSI and NoRH light curves. The resultant wavelet power spectra are shown in Fig. 2(c,d). Again the 3-min periodicity is seen to be significant in both the wavelet spectra above the 99% confidence level, which is consistent with the periodogram analysis.

We generated the X-ray spectrum obtained with RHESSI during 23:53-23:54 UT using the OSPEX package in SSWIDL (Figure 3). The background-subtracted

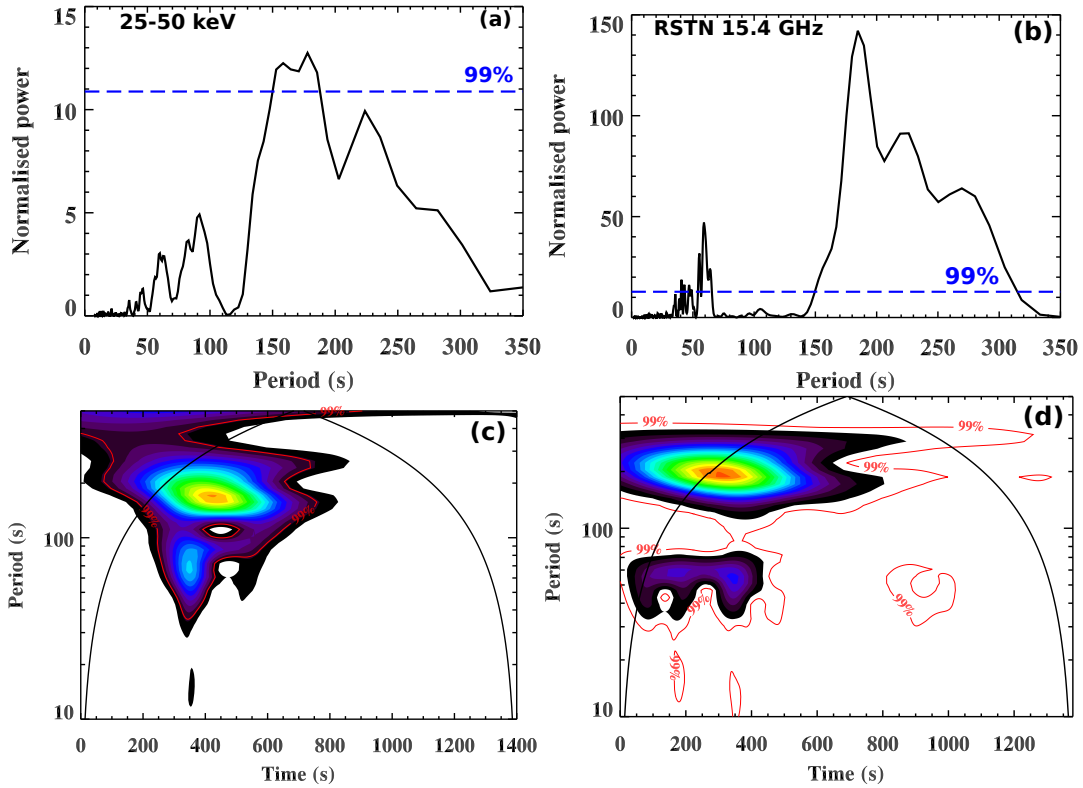

FIG. 2.— (a-b) Lomb–Scargle periodograms of RHESSI 25–50 keV and RSTN 15.4 GHz signals. (c-d) Wavelet power spectra for RHESSI 25–50 keV energy channel (left) and RSTN 15.4 GHz (right) signals. The start time is 23:48 UT.

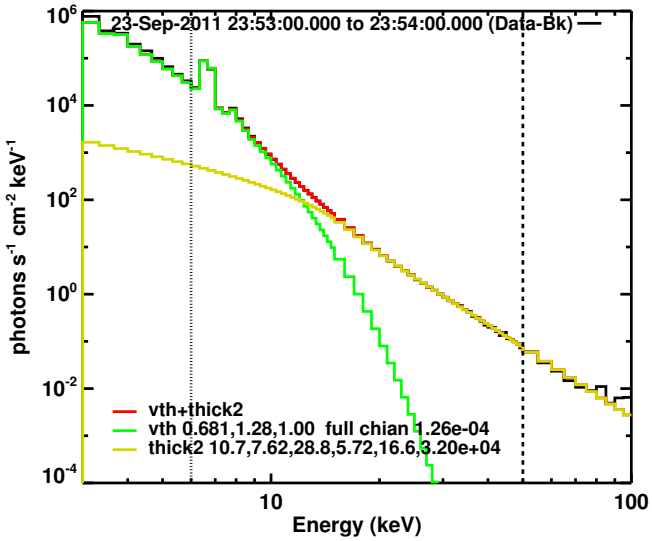

FIG. 3.— RHESSI energy spectrum fitted with the isothermal (green) and thick-target bremsstrahlung (yellow) models for the interval 23:53–23:54 UT.

photon flux is fitted with thermal (green) and nonthermal (yellow) components. We used an isothermal component (V_{th}) for the optically thin thermal bremsstrahlung radiation and thick target bremsstrahlung version-2 model (thick2) for the nonthermal photon flux due to the interaction of accelerated electrons with the thick target plasma. We chose 6–50 keV energy range indicated by vertical dotted lines, for the fitting purpose. From the best-fitting parameters, we derived the temperature T and emission measure (EM) of the hot plasma to be 14.8 MK and 0.68×10^{49} cm^{-3}, respectively. The spectral index for the thick-target bremsstrahlung is 5.7. The nonthermal component dominates over the thermal component above ∼13 keV. Therefore, it is clear that the observed QPP is basically related to the periodic variation of the nonthermal electron flux.

2.2. *Spatial location of the hard X-ray and radio sources*

To investigate the particle precipitation/transport sites during the flare, we used hard X-ray 25–50 keV and NoRH 17/34 GHz images. We chose the PIXON algorithm (Metcalf et al. 1996) for the RHESSI image reconstruction. The pixon method is considered to be the most accurate algorithm (Hurford et al. 2002). The integration time for each image was 20 s. We utilised NoRH 5-s cadence intensity images (R+L) at 17 and 34 GHz. Figure 4 displays the hard X-ray 25–50 keV (blue) and NoRH 17 GHz (red) contours overlaid on the AIA 1,600 Å images at ∼23:51 UT. These images are used at the peak time of each of the bursts observed in the hard X-ray 25–50 keV and microwave channels. Figure 4(a) shows a small filament rising at the flare site. We can easily identify the two legs of the filament (marked by N and S in the figure). Generally, the filaments are observed in the chromospheric images (e.g., Hα and AIA 304 Å. However, if the kink unstable filament is heated during magnetic reconnection, it is often observed in the AIA 1600 Å channels (e.g., Kumar et al. 2012 and Kumar & Cho 2014). The locations of both the 25–50 keV sources and 17 GHz source are almost at the quasi-circular ribbon. However, their centroids constructed at the 90% level of the peak intensity are not cospatial. We note that the 25–50 keV sources (centroid) are located close to the legs of the filament, whereas 17 GHz source is located at the

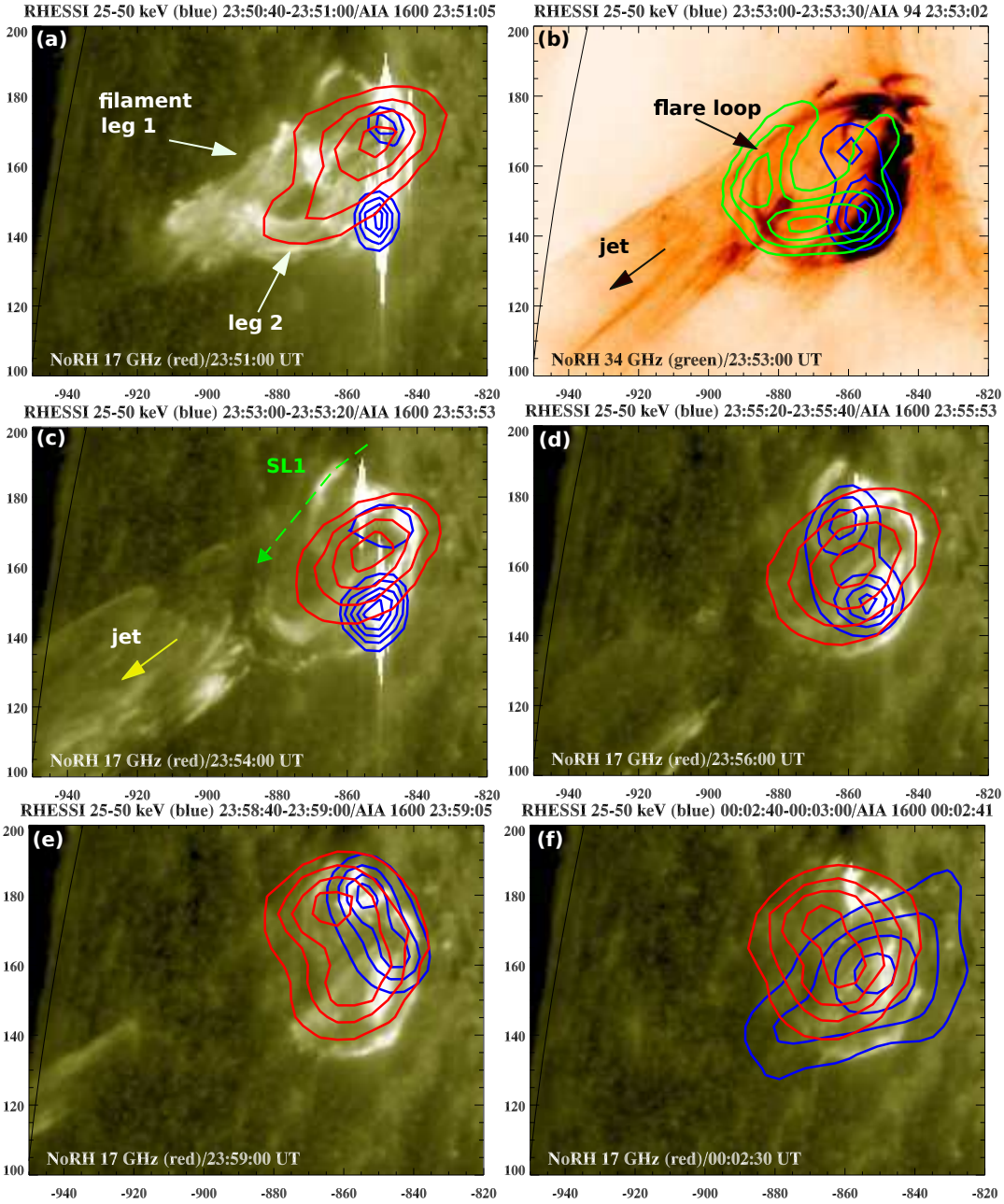

FIG. 4.— RHESSI hard X-ray (25–50 keV, blue) and NoRH (R+L) 17 GHz sources shown by the contours overlaid on the AIA 1,600 Å images. Panel (b) shows RHESSI 25–50 keV (blue) and NoRH 34 GHz (green) contours over the AIA 94 Å negative image. The time of each image matches the peak time of the 3-min oscillation in the hard X-ray 25–50 keV and radio 17 GHz. The contour levels are 30%, 50%, 70%, 90% of the peak flux. We included an extra contour level (i.e., 10% of the peak flux in panel (c)) to show the opposite foot-point of the loop. The axes are labelled in arcsecs.

northern leg of the filament. It seems that these sources are at the footpoints of an underlying flare loop. To identify the location of the flare loop, we selected the AIA 94 Å hot channel image at 23:53 UT. In this image (panel b), we showed NoRH 34 GHz contours (yellow) overlaid on AIA 94 Å images at ∼23:53 UT. This is done to show the coronal loops associated with the eruption of the small filament. The overlying 34 GHz source is cospatial with the small loop located above the quasi-circular ribbon. This 34 GHz emission may be the evidence of trapped nonthermal electrons in the loop. The rising filament is heated during reconnection with the ambient fields, and then decays into an untwisting jet as seen in Fig. 4(b-e). Furthermore, during ∼23:53-23:59 UT, we see the footpoint hard X-ray sources. The NoRH 17 GHz sources cover the quasi-circular ribbon (Figure 4(c-d)) and could be the emission from the trapped electrons in the loop. This suggests that the bursts are most likely caused by the same population of nonthermal electrons with different energies.

2.3. *Magnetic configuration*

To investigate the magnetic configuration of the flare site, we used Hinode/SOT (Tsuneta et al. 2008), XRT

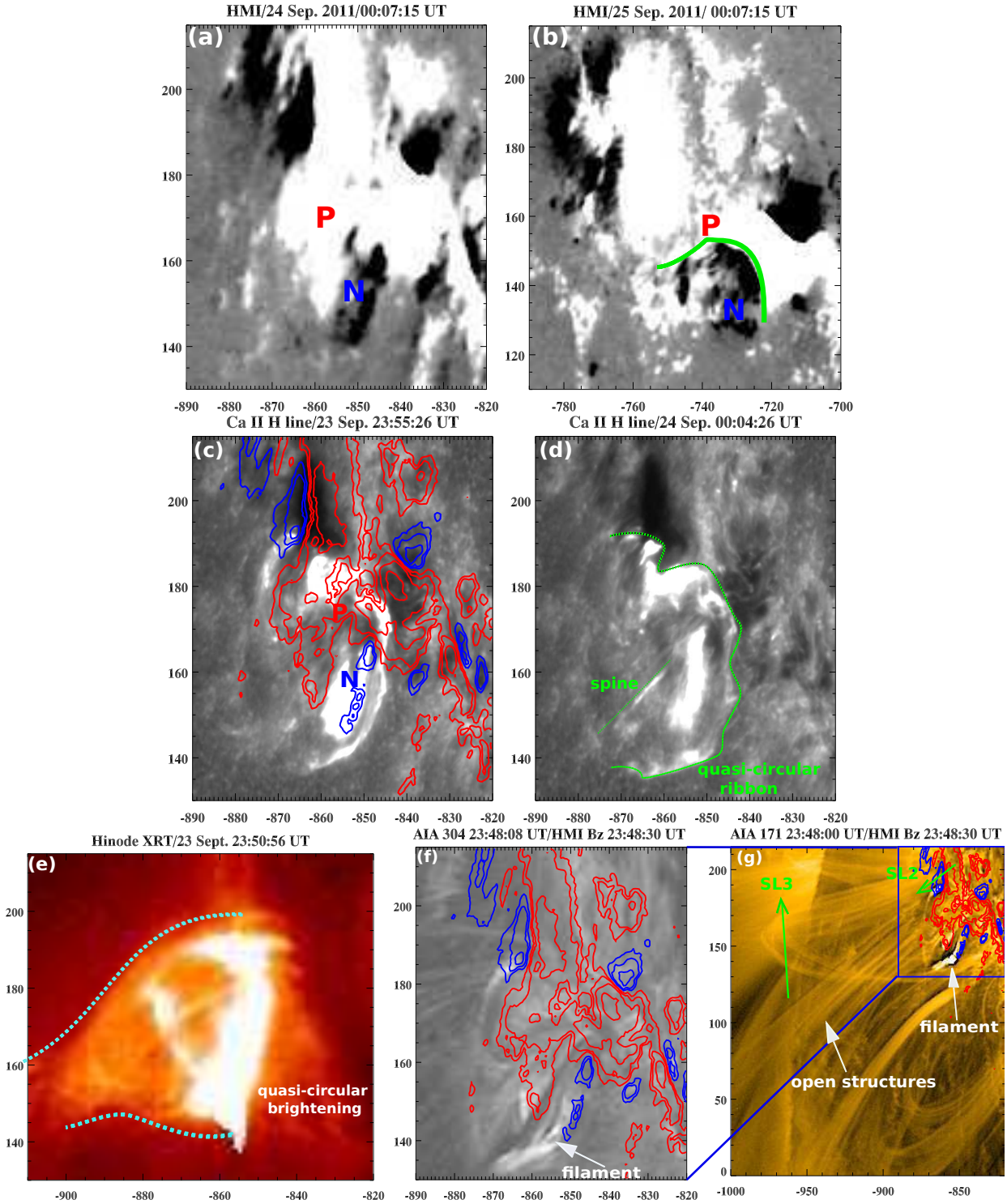

FIG. 5.— (a-b) HMI magnetogram of the flaring AR on 24 and 25 September 2011. P and N indicate positive and negative polarity fields. Green line is the PIL. (c-d) Hinode/SOT Ca II H line (3968 Å) images showing the flare ribbon morphology. (e-g) XRT image (Be_thin filter) during the flare onset showing the magnetic configuration and formation of quasi-circular brightening at the foot-points of the loops. AIA 304 and 171 Å images overlaid by HMI magnetogram of positive (red) and negative (blue) polarities. The contour levels are ±200, ±400, ±800, and ±1,600 G.

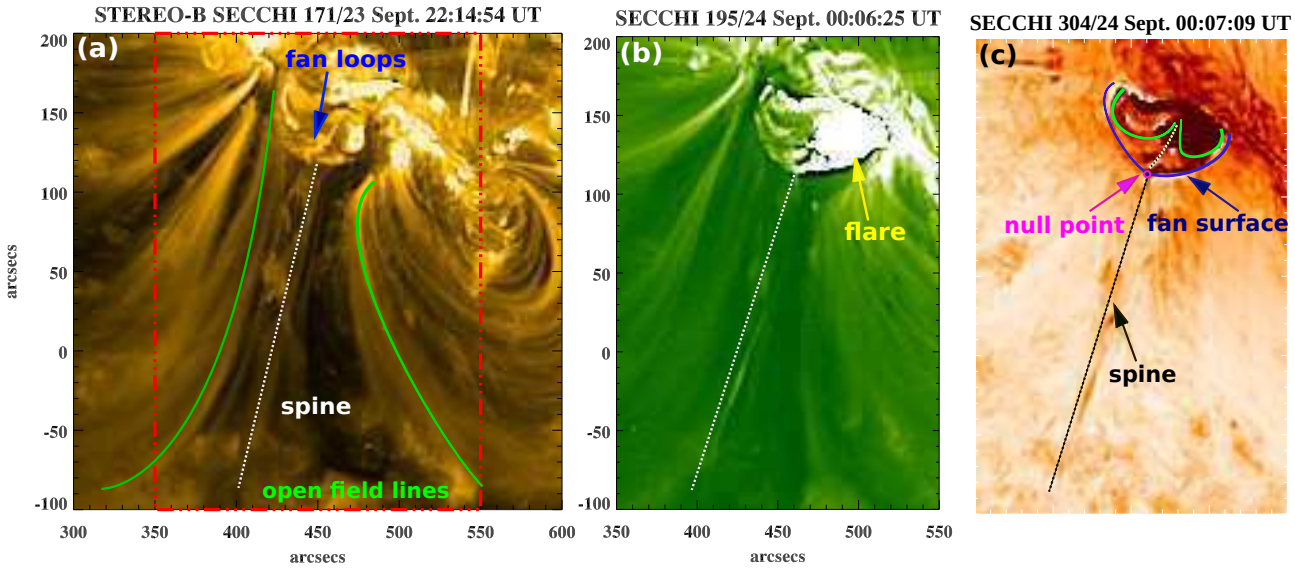

FIG. 6.— STEREO-B SECCHI intensity images in 171, 195, and 304 (reverse colour) Å channels. These images display the possible magnetic configuration (i.e., fan-spine topology) of the flare site. The rectangular box in panel (a) indicates the location of the field-of-view in panels (b) and (c).

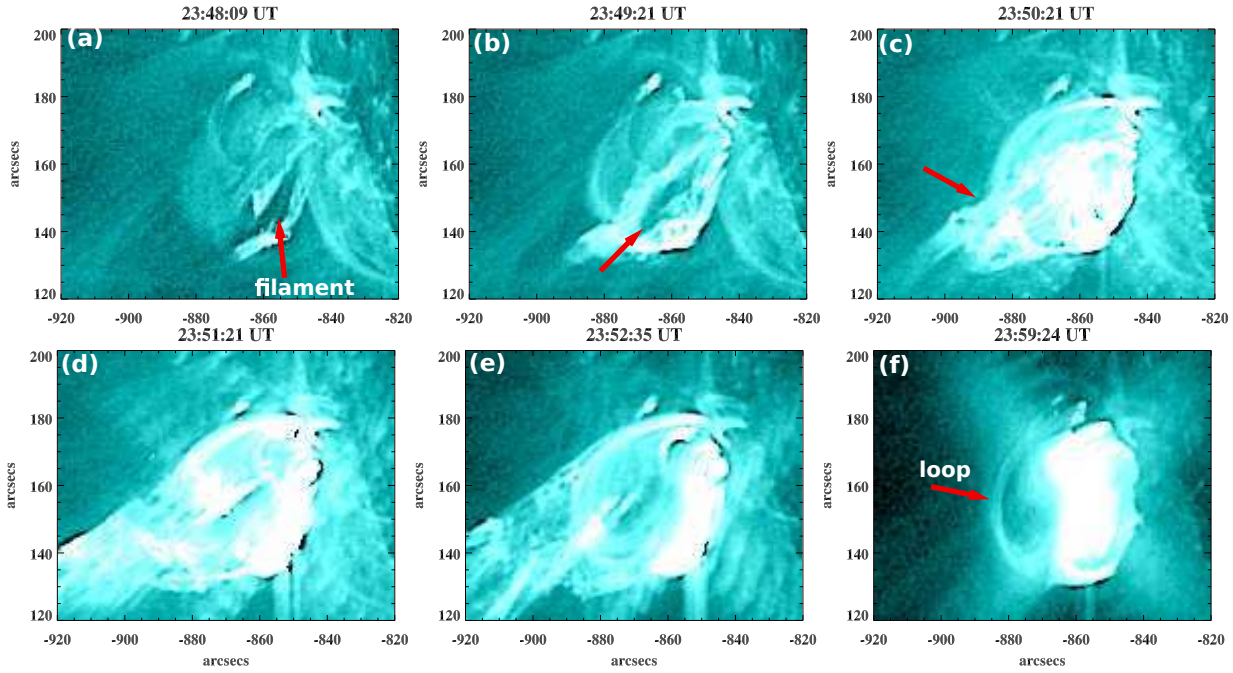

FIG. 7.— Selected AIA 131 Å images showing the filament rise, its interaction with the pre-existing field, and associated plasma heating. (An animation of this figure is available.)

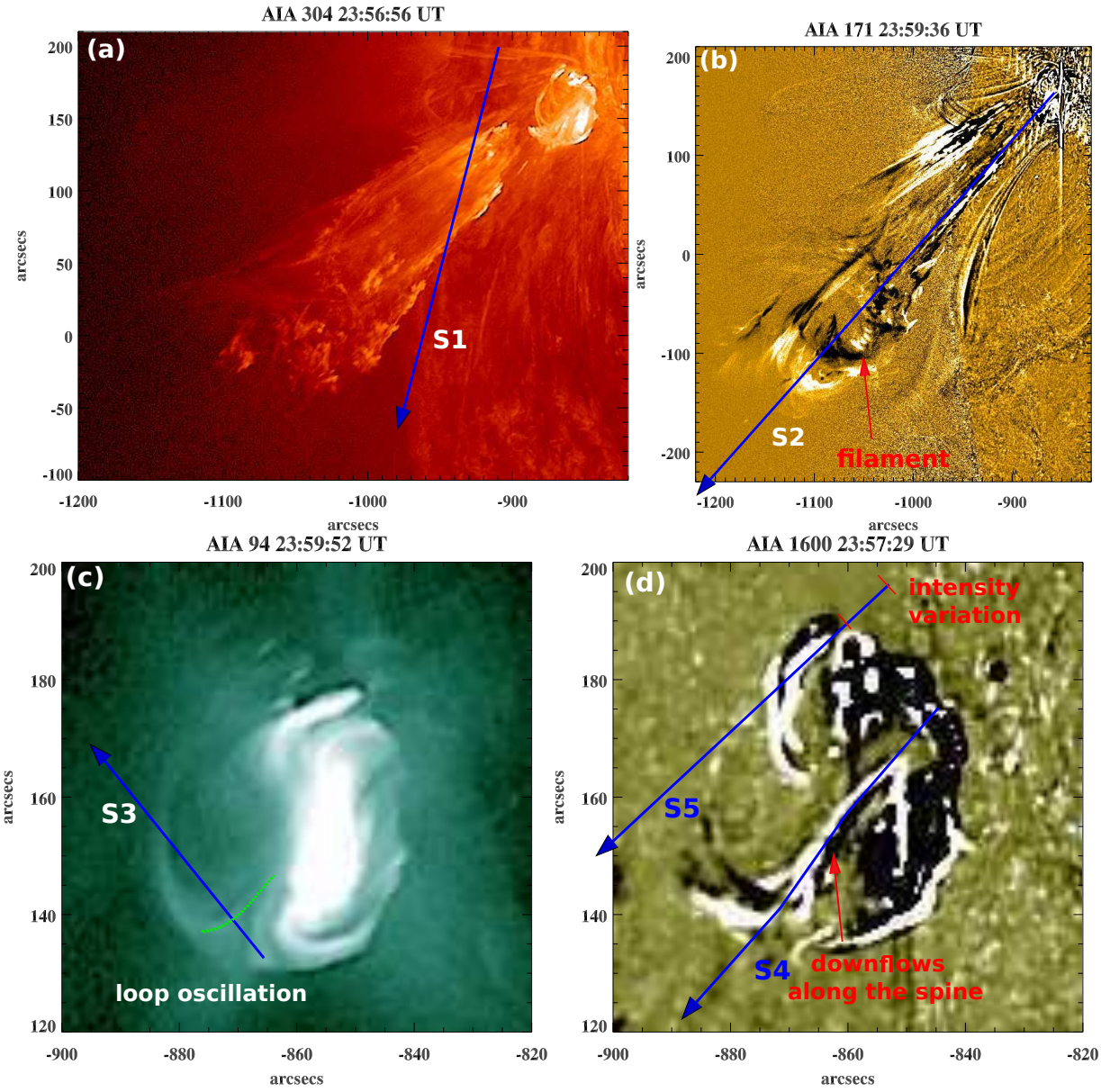

FIG. 8.— AIA 304, 171, 94 and 1,600 Å images during the flare. S1, S2, S2, S4, and S5 are the slice cuts used to create the time-distance plots. Arrow head indicates the direction of the cut for the time-distance plots. (An animation of this figure is available.)

(Golub et al. 2007), SDO/HMI and AIA images. Figure 5(a,b) displays HMI magnetograms of the flaring active region on 24 Sepetember (left) and 25 September 2011 (right). Since the active region was close to the eastern limb, therefore, some of the magnetic polarities at the edge of big sunspot may not be true. We carefully checked the magnetic polarities after 24 September when the active region was closer to the disc center. At the flare site, we observe negative polarities (N) surrounded by the positive polarity region (three sides). The arc shaped PIL is marked by the green line. The M-class flare occurred at the edge of the active region. The Ca II H line images (Figure 5(c,d)) show a quasi-circular flare ribbon. Circular or quasi-circular flare ribbons generally indicate the presence of a fan-spine topology at the flare site (Masson et al. 2009; Pariat et al. 2010; Wang & Liu 2012; Cheung et al. 2015; Kumar et al. 2015). We also noticed the presence of bright upflows along the possible spine (marked by the dotted line) in the chromosphere. Figure 5(e) displays the Hinode XRT image (Be_thin, log T∼6.8-7.0 MK) during the flare onset (23:50:56 UT). Interestingly, we see quasi-circular brightening at the footpoints of the loops. The AIA 304 Å image (Fig. 5(f)) shows a small filament lying along the neutral line. The AIA 171 Å image reveals open field lines with a possible fan-spine topology at the eruption site (Fig. 5(g)). These images are overlaid by the HMI magnetogram contours of positive (red) and negative (blue) polarities.

The Solar TErrestrial RElations Observatory (STEREO) SECCHI-B (behind, Wuelser et al. 2004; Howard et al. 2008) observed the same active region close to the disk center. Therefore, it provides an opportunity to visualise the 3D structure of the active region loops. Also, SECCHI observed the flare and jet-like

eruption of the filament material along the open field lines. Figure 6(a) displays the active region in the 171 Å channel before the flare onset (at 22:14:54 UT). We can see the fine structure and connectivity highlighted by different loops within the active region. We assume fan-loops with an outer spine at the flare site. On the basis of these observations, we draw (over the image) open field lines and an outer spine at the eruption site. In Fig. 6(b), we display an SECCHI 195 Å image showing the flare and associated plasma flow along the outer spine at 00:06:25 UT. Similar fan loops and the plasma motion along the outer spine was observed in the SECCHI 304 Å (reverse colour) image (00:07:09 UT). The schematic cartoon of the fan-spine topology including a possible 3D null point is shown in Fig. 6(c). The development of the filament resulted in eruption that followed the open field line along the outer spine and produced a CME in the interplanetary medium.

2.4. *Trigger of the oscillation*

Figure 7 displays several selected images taken in the AIA 131 Å channel. The 131 Å channel is sensitive to both hot ($T \approx 10$ MK) and cool plasma ($T \approx 0.4$ MK). Before the flare, we see a small filament (at ∼23:48 UT) lying below the fan-loops. The flare brightening starts with the rise of the filament (at 23:49:21 UT). The filament interacted with the overlying preexisting fields. The ejection of the filament is similar to the blowout jet scenario (e.g., Moore et al. 2015). The filament material showed an untwisting motion during the eruption. We also noticed a transverse oscillation of a small loop above the flare centre (Fig. 7(f)).

To study the untwisting motion of the erupting filament, its speed, the kink oscillation of the small loop, and the associated downflows along the spine at the flare site, we used slice cuts S1, S2, S3, S4, and S5 made in the AIA 304, 171, 94, and 1,600 Å images (Figure 8). Fig. 8(a,b) show the filament material ejected from the flare site in the AIA 304 Å intensity and 171 Å running difference images. Cut S1 is used to detect the untwisting/rotation of the filament material, whereas cut S2 is used to visualise the outward plasma ejections during the periodic energy release. The direction of the slice cut is marked by the arrowhead at the end of the slice. Fig. 8(c) shows the AIA 94 Å intensity image for the slice cut S3. Cuts S4 and S5 in the AIA 1,600 Å (running difference) image are used to detect the plasma downflows along the spine (Fig. 8(d)).

Figure 9(a,b) displays the stack (running difference intensity) plots along the slice S1 using sets of the AIA 304 and 171 Å images. We see the periodic brightening in these plots, which may be associated with the untwisting motion of the filament plasma. The bright propagating features in the stack plot shows the tangential motion of the plasma. To see the temporal association of these untwisting motions with the periodic energy releases, we overplotted the RHESSI hard X-ray flux (25–50 keV, blue curve) in panel (a). Interestingly, we see a good temporal correlation of the untwisting motion with the hard X-ray bursts with a 3-min period. The periodic brightening has an approximately 3-min period similar to the hard X-ray emission. The linear/tangential speeds of untwisting features 2, 3, and 4 (blue dotted lines) are ∼256, ∼235, and ∼130 km s^{-1} respectively. The average speed is ∼207 km s^{-1}. The careful investigation of Fig. 9(b) reveals an additional co-temporal untwisting motions in the bottom side of the stack plots. It is clear that the upper part (U) of the jet shows counterclockwise motion, whereas the lower part (L) of the jet reveals the clockwise rotation. These oppositely directed untwisting motions may be a signature of a torsional Alfvén wave embedded in the filament material.

Fig. 9(c) shows the erupting plasma motion along slice S2. The projected speed of the outward moving plasma was ∼632 km s^{-1}. Note that there are five distinct ejections. After interacting with the overlying fields, the filament showed impulsive acceleration.

In Fig. 9(d), we display the stack plot along the slice S3 using 94 Å intensity images. It shows that the filament rise was followed by a transverse oscillation of the small loop located above the flare centre. To see the association of the kink oscillation with the observed periodic particle acceleration, we determine the oscillation period as ∼230±10 s (i.e., about 4 min). The oscillation period is not consistent with the period of the detected QPP in the energy release. Therefore, it is unlikely that this kink oscillation of the small loop could trigger the periodic reconnection. The oscillations were observed mainly in the loop leg where we noted the downflows along the vertical spine field observed in the AIA 1600 Å. It seems that the loop oscillation is triggered by the unstable filament.

To see the quasi-periodic energy release and associated downflows in the EUV, we used AIA 1,600 Å images. Fig. 9(e) shows the mean 1,600 Å intensity obtained by averaging the signals of individual pixels in a box that covers the flare ribbon. The quasi-periodic energy release observed in this channel is quite similar to the hard X-ray emission (25–50 keV). The emission observed in the AIA 1,600 Å channel is basically generated by the periodic precipitation of the nonthermal electrons propagating downward from the reconnection site. The periodic downflows are also observed along the spine (Fig. 9(f)). The speed of these downflows is ∼60, ∼84, and ∼52 km s^{-1}, respectively. The lower end of slice S5 covers a sunspot north to the flare ribbon. The running difference intensity plot clearly shows the periodic variation of the intensity (between the horizontal red dotted lines) generated by the precipitation of energetic particles. The variation of the average intensity between the red dotted horizontal lines is overplotted in panel (g). This finding indicates that leakage of sunspot oscillations could periodically trigger magnetic reconnection.

2.5. *Wave trains*

In addition, in the AIA 171 Å channel we observed a rapidly propagating wave train. The AIA 171 Å running movie shows the wave train of the intensity variation during 00:06–00:18 UT, propagating in the southward direction. To determine the apparent speed of the wave train, we chose a curved path along the propagating wave train in the AIA 171 Å image (Figure 10(a)). Fig. 10(b) displays the stack plot of running difference intensity along the selected path. We see the propagating wave train starting at 00:06 UT. The individual wavefronts are marked by 1, 2, 3, 4, and 5. We chose the second wavefront (blue dotted line) to determine the

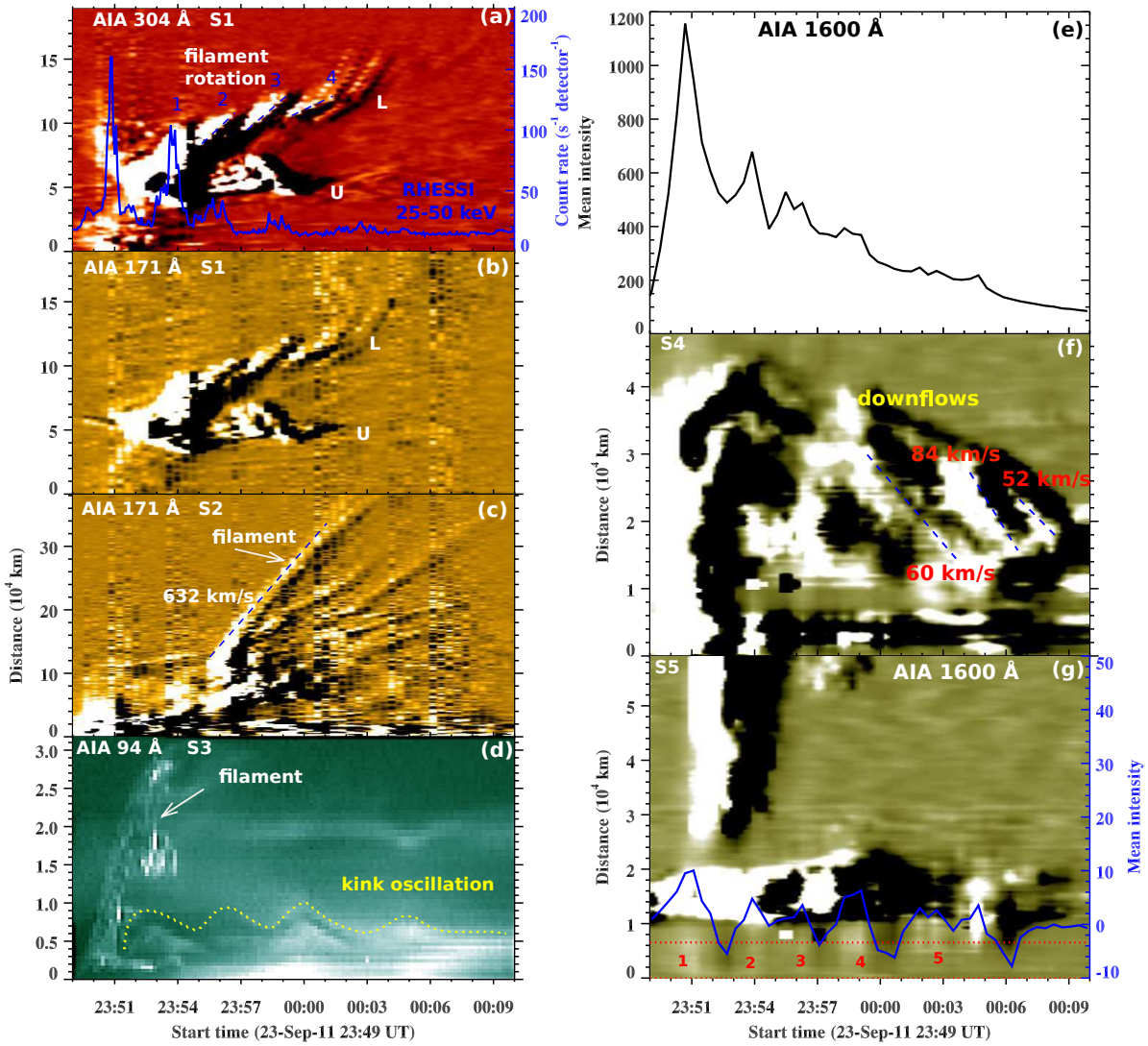

FIG. 9.— (a-d) Time-distance intensity plots along slices S1, S2, and S3 using AIA 304, 171, and 94 Å images. AIA 304 and 171 Å plots are created from the running difference images with the time of 1 min between the images; while the AIA 94 Å plot is made from the intensity images. The blue curve is the RHESSI hard X-ray flux profile in the 25–50 keV channel. U and L are the upper and lower parts of the jet structure. (e) The AIA 1,600 Å mean intensity profile extracted from the box 1. (f-g) AIA 1,600 Å time-distance running difference intensity plots along the slices S4 and S5. The blue curve shows the mean intensity extracted between two red horizontal dotted lines.

speed, as this wave front was the most pronounced one. The average projected speed of the front was found to be ∼320±27 km s^{-1}. The period of the filling signal in the wave train is ∼2.2 min.

The speed of the individual fronts in the wave train is not so high as observed in the previous flares (Liu et al. 2012; Kumar & Manoharan 2013; Pascoe et al. 2013). The fast wave trains usually have higher speeds, ∼1000–2000 km s^{-1}, measured during the impulsive phase of a flare. In our case, we observed the wave train during the flare decay phase (00:06–00:18 UT). It is unclear why these wave-trains are not observed during the flare impulsive phase. However, the estimated projected speed of the wave train in our case is consistent with the result of Liu et al. (2012) who observed lateral deceleration of a wave train from ∼650 to 340 km s^{-1}.

Let us assume that the wave train is generated during the periodic energy release. The time difference between the start time of the hard X-ray burst and the appearance of the wave trains is ∼15 min. The distance of the observed wave train from the flare energy release site is ∼300″. Let us assume that the initial speed of the wave train equals to the filament material speed ∼632 km s^{-1}. The time taken by the wave train to reach the observed distance will be ∼6 min. The estimated time is much smaller than the actual time difference from hard X-ray bursts. Therefore it is unlikely that the wave trains are generated during the flare impulsive energy release.

2.6. *Sunspot oscillations and kink oscillations of the 171 Å arcade loops*

To investigate the relationship between sunspot oscillations and associated periodic energy release, we selected slices SL1 and SL2 (AIA 1,600 Å and 171 Å images shown in Fig. 4(c) and Fig. 5(f)) at the sunspot located at the eruption site. The running difference intensity

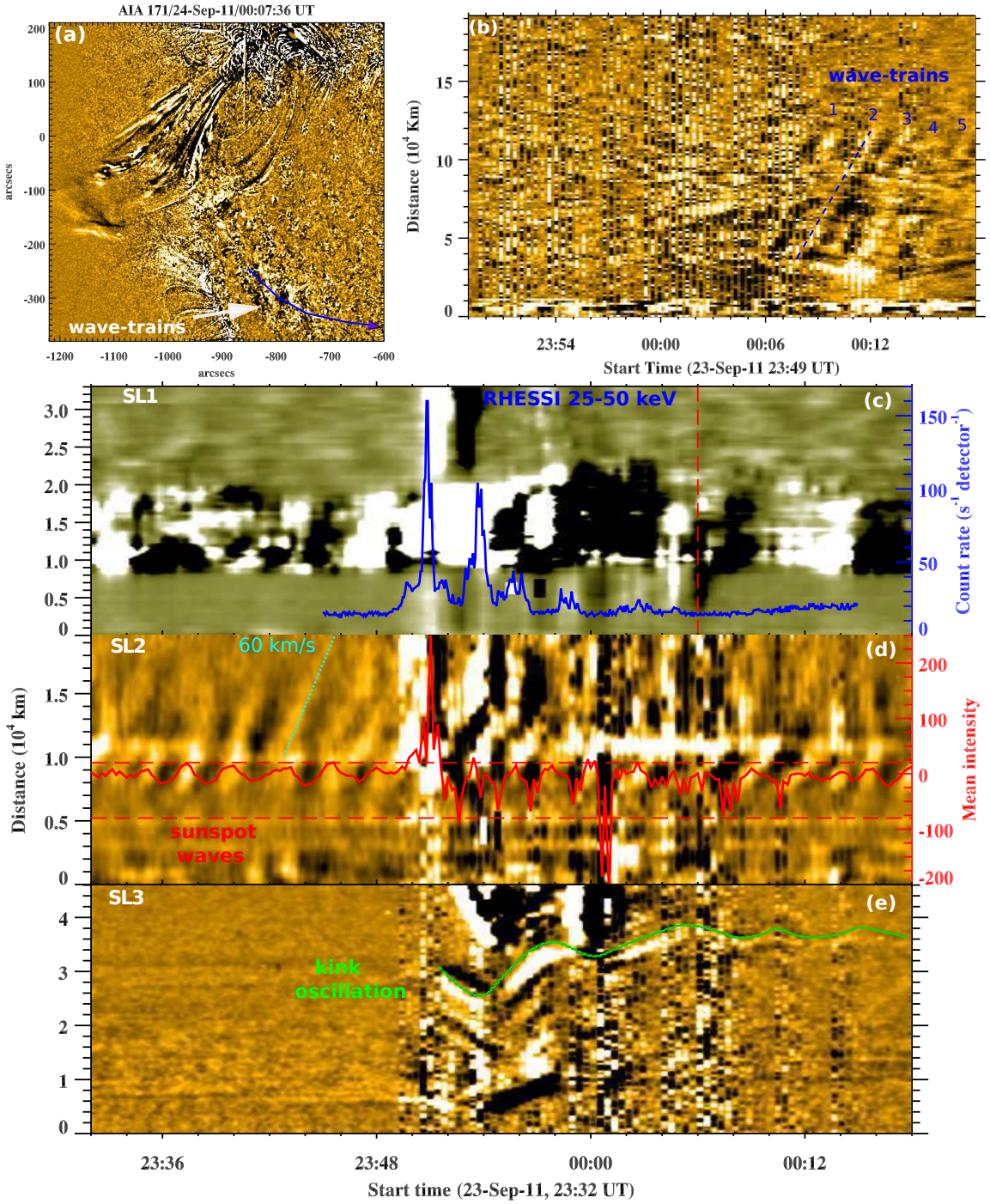

FIG. 10.— (a) AIA 171 Å running difference image showing a rapidly-propagating wave train (b) Time-distance intensity (running difference) plot along the selected path (blue) shown in panel (a). (c) Stack plot of the AIA 1,600 Å running difference intensity along slice SL1 shown in Fig. 4(c). Blue curve is the RHESSI hard X-ray flux profile in the 25–50 keV channel. The vertical dotted line (red colour) shows the appearance of the wave train in the AIA 171 Å channel. (d, e) Stack plots of the AIA 171 Å running difference intensity along the slices SL2 and SL3 (refer to Fig. 5(f)) showing 3-min waves leaking from a sunspot and the 6-min kink oscillations (green) of the overlying arcade loops, respectively. The red curve shows the mean intensity extracted between two horizontal lines shown in the middle panel. (An animation of this figure is available.)

along these cuts (SL1, SL2) during 23:32–00:18 UT is plotted in Fig. 10(c, d). The AIA 1,600 Å movie reveals the repeated umbral flashes before the flare onset at 23:32 UT onward. Interestingly, we noticed the increase in the umbral intensity by the periodic precipitation of nonthermal electrons during the flare, which is cotemporal with the RHESSI hard X-ray flux (25–50 keV, blue curve). Since the intensity change (marked in Fig. 8(d)) is consistent with the AIA 1600 mean intensity profile and HXR profile, therefore, it is likely that the intensity change could be a result of particle precipitation near the sunspot. However, we also observed the leakage of the slow-mode waves co-temporally in the AIA 171 channel (Fig. 10(d)).

Fig. 10(d) shows the propagating EUV disturbances, going from the sunspot along slice SL2 (AIA 171 Å). Their apparent (i.e., projected) speed is subsonic for the temperature associated with these EUV channels, and hence they are interpreted as slow magnetoacoustic waves (de Moortel 2009). In our case, the apparent speed of a front is ∼60 km s^{-1} (Fig. 10(d)). The average intensity (running difference) has been extracted from the 171 Å stack plot (between two horizontal dashed lines) and overplotted in the same panel (red curve). A comparison of the timing of sunspot oscillations with the RHESSI hard X-ray flux profile suggests a high correlation between them. Therefore, it is very likely that the reconnection is periodically modulated by the slow-mode waves leaking from the sunspot. The possible leakage of umbral oscillations in the corona along magnetic field lines in a form of slow-mode waves has been demonstrated in (Botha et al. 2011). The slow-mode waves can reach the reconnection site in the fan-spine topology and periodically trigger the energy release by the mechanism described by Chen & Priest (2006); Sych et al. (2009).

Furthermore, we also noticed a kink oscillation of the overlying arcade loops at the eruption site. Fig. 10(e) shows the running difference intensity plot along slice SL3 in the AIA 171 image (Fig. 5(f)). During the first hard X-ray burst, we see the contraction of the arcade loops followed by decaying kink oscillations. The oscillation period is ∼6 min. The oscillation was possibly triggered by the erupting jet-like structure of the untwisting filament. Alternatively, the contraction of the cool arcade loops may be due to the decrease in the magnetic pressure at the flare site as a result of the magnetic energy release during the flare (Hudson 2000).

2.7. *Coronal Mass Ejection*

The jet-like eruption of the small filament produced a CME, which was observed during the event by the SOHO/LASCO coronagraph (Brueckner et al. 1995; Yashiro et al. 2004). The CME frontal loop appeared at 00:12:06 UT in the LASCO C2 field of view. The CME speed (from LASCO CME catalog[1]) was ∼617 km s^{-1}, which is close to the filament material speed (∼632 km s^{-1}) in the low corona (Fig. 9c). The CME does not show significant deceleration (2.83 m s^{-2}) up to ∼20$R_\odot$ in the interplanetary medium.

3. SUMMARY AND DISCUSSION

We presented multi-wavelength observations of 3-min QPP in a solar flare, detected simultaneously in the hard X-ray, radio and EUV channels. Recently, Kumar et al. (2015) observed a decaying oscillation in the flaring emission, with three distinct peaks in the X-ray (6–12 keV) channel observed by the Fermi GBM (Gamma-ray Burst Monitor). Here we observed decaying oscillations in the RHESSI hard X-ray channel (25-50 keV) with five distinct peaks without any gradual broadening in the burst profile. Specific results of this study are summarised below:

(1) We observed a quasi-circular ribbon during the flare, which suggests a fan-spine magnetic topology of the flare site (see Masson et al. 2009; Pariat et al. 2010; Pontin et al. 2013; Kumar et al. 2015, for discussion). In Masson et al. (2009), the outer spine is connected to a remote ribbon. Non-thermal electrons accelerated at the reconnection site, propagate downwards along the fan loops and upward along the outer spine. A circular or quasi-circular ribbon is generated by the precipitation of nonthermal electrons downward along the fan loops. If the outer spine is connected within the active region (i.e., closed), we should observe a remote ribbon as a result of confined electrons along the outer spine/arcade loops that precipitate at the opposite footpoint. The formation of a remote ribbon within the active region with a fan-spine topology suggests the closed spine (e.g., Masson et al. 2009; Kumar et al. 2015). If the outer spine is open (Pariat et al. 2010), we generally do not expect a remote ribbon associated with the outer spine. In addition, we should observe the type III radio bursts suggesting the injection/escape of nonthermal electrons (into the IP medium) along the open field lines. The hard X-ray sources (25-50 keV) which we observe are close to the footpoints of the kinked filament and within/at the quasi-circular ribbon. We also observed open structures in the AIA 171 Å and STEREO images emanating from the flare site. A 3-D model of solar jets with a fan-spine topology including a magnetic null and open outer spine is proposed by Pariat et al. (2010). Our case study does not show a remote ribbon (within the AR) associated with outer spine. We only observed a quasi-circular ribbon and periodic type III radio bursts. Therefore, it indicates that the magnetic configuration (in our case) is most likely a fan-spine topology where the outer spine is open (similar to Pariat et al. 2010).

In addition, we noted the untwisting motion of a filament material with an almost 3-min period. Therefore, the rising filament interacts with the overlying pre-existing field and can periodically trigger magnetic reconnection at the null point resulting in quasi-periodic injection of nonthermal electrons toward the footpoints of the fan loops leading to the formation of quasi-circular ribbons.

(2) The presence of periodic type III radio bursts suggests the propagation of nonthermal electrons along the open field lines. This means that the outer spine is extended into the interplanetary medium (i.e., open field lines at the eruption site) and not connected to the remote site within the active region as was observed by Kumar et al. (2015). Note that Kumar et al. (2015) did not observe type III radio bursts in the interplanetary medium because of the possible confinement of the

[1] http://cdaw.gsfc.nasa.gov/CME_list/UNIVERSAL/2011_09/htpng/20110924.001206.p108g.htp.html

accelerated (nonthermal) electrons in the arcade loops (i.e., no escape into the interplanetary medium) within the active region. Moreover, the formation of a remote ribbon along with heating of the arcade loops (131 and 94 Å channels) suggests the precipitation of nonthermal electrons toward the the opposite footpoint of the heated arcade loop, which produced a 3-min EUV QPP similar to that observed in the X-ray channel. In addition, the oscillation event studied by Kumar et al. (2015) showed a failed eruption of an untwisting small filament that interacted with the fan-spine magnetic field configuration. The absence of longer hot arcade loops that could be visible in 131 and 94 Å channels, in our event confirms that the particles are not accelerated/transported (along the closed spine/arcade loops) from the flaring footpoint to the opposite footpoint (i.e., remote ribbon) in the active region. Therefore, magnetic topology is open, allowing to produce periodic type III radio bursts. In addition, in this study we observed a successful eruption of a small filament leading to a CME observed by the LASCO C2 coronagraph.

(3) This event does not reveal a slow-mode wave propagating back and forth along the hot arcade loops as reported by Kumar et al. (2013, 2015). Therefore, we can rule out the trigger of periodic reconnection by a slow-mode wave reflecting back and forth between the footpoints of the hot arcade loops. In fact, the periodic reconnection may be induced by the untwisting motion of the small filament (not by a reflecting longitudinal wave in the hot arcade loops). The rising filament reconnects with the pre-existing fields, and then gets destroyed to form a jet-like structure.

(4) This study also highlights the origin of the blowout jets observed in the coronal holes, which generally reveals an untwisting motion during the eruption (Moore et al. 2015). However, properties of the coronal hole blowout jets are quite similar to the active region jets originating in the fan-spine topology. This untwisting motion is generally observed during the interaction of a kink-unstable flux rope with the pre-existing ambient field. One leg of the flux rope can be detached as a result of reconnection that leads to the unwinding/untwisting motion of the flux rope (Kumar et al. 2012; Kumar & Cho 2014; Kumar et al. 2015).

(5) The observed 3-min QPP are most likely triggered by slow-mode waves leaking form a nearby sunspot. The waves may be guided by the legs of the untwisting filament, and trigger periodic reconnection at the null point by the mechanism proposed in Chen & Priest (2006). We observed a good temporal correlation between the sunspot waves and HXR QPP. A similar scenario of the leakage of sunspot oscillations in the corona, and periodic triggering (modulation) of flaring energy release was discussed in Sych et al. (2009).

(6) We observed kink oscillations of a small loop (131 and 94 Å) at the flaring site, with a period of ∼4 min. In addition, we also observed kink oscillations of the overlying arcade loops (period ∼6 minute). The kink oscillation period does not match the period of the observed QPP (∼3 minute). Therefore, we can rule out the modulation of the periodic reconnection by the kink oscillation of the nearby loops, and consider the kink oscillations as a response of the coronal fast-mode (kink) MHD resonators to the flaring energy release. However, the wave train observed in this event may be generated by the periodic magnetic reconnection.

(7) The eruption of a flux rope can launch Alfvén waves in the opposite direction (up and down) along the flux rope/filament and can generate a vortical motion at the footpoints in the photosphere (Longcope & Welsch 2000; Fan 2009). Signatures of the torsional Alfvén waves have been detected in the small flux rope structures observed in the interplanetary medium (Gosling et al. 2010). In addition to the previous findings, our case study shows an untwisting motion of the filament material with almost the same period (∼3 min) as the observed QPP. Moreover, we also noticed rotations in the opposite directions of two structures in the same jet. Very recently, Lee et al. (2015) performed a numerical simulation of helical blowout jets in an emerging flux region. They found that (i) the untwisting motion had been a result of reconnection of the twisted emerging magnetic field with a pre-existing field, (ii) untwisting motion was associated with the propagation of torsional Alfvén waves in the corona. In addition, Moore et al. (2015) reported magnetic untwisting in polar coronal hole jets and suggested the magnetic untwisting wave to be a large amplitude (nonlinear) torsional Alfvén wave. On the basis of the above arguments, we speculate the possibility of a torsional Alfvén wave in the jet-like structure. If we accept this option, it is possible that the oppositely directed Alfvén waves in the untwisting jet could accelerate the electrons bidirectionally with 3-min period. Alternatively, the torsional waves propagating along the flux rope could change the direction of the field lines to generate a favourable condition for periodic magnetic reconnection between the emerging twisted and pre-existing field (Ning et al. 2004). The generation of torsional waves during reconnection and associated particle acceleration mechanism in solar flares have been proposed by Fletcher & Hudson (2008).

In conclusion, we reported the possible manifestation of periodic injection of non-thermal electrons bidirectionally in a fan-spine topology during an M-class flare. The acceleration could be periodically modulated by the leakage of sunspot oscillations or by the untwisting motion of a small filament lying under the fan loops. Similar events should be investigated in more details to reveal the exact trigger mechanism of QPPs in solar flares.

We would like to thank the referee for the positive and constructive comments that improved the manuscript considerably. SDO is a mission for NASA Living With a Star (LWS) program. This work was supported by the "Development of Korea Space Weather Center" of KASI and the KASI basic research funds. The SDO data were (partly) provided by the Korean Data Center (KDC) for SDO in cooperation with NASA and SDO/HMI team. RHESSI is a NASA Small Explorer. Nobeyama radioheligraph and polarimeters are operated by the National Astronomical Observatory of Japan (NAOJ)/Nobeyama Solar Radio Observatory (NSRO). Hinode is a Japanese mission developed and launched by ISAS/JAXA, with NAOJ as domestic partner and NASA and UKSA as international partners. It is operated by these agencies in co-operation with ESA and NSC (Norway). PK thanks

Bindu Rani for helpful discussions. K.-S. Cho acknowledges support by a grant from the US Air Force Research Laboratory, under agreement number FA 2386-14-1-4078 and by the "Planetary system research for space exploration" from KASI. VMN acknowledges the support from the European Research Council under the *SeismoSun* Research Project No. 321141, STFC consolidated grant ST/L000733/1, and the BK21 plus program through the National Research Foundation funded by the Ministry of Education of Korea. Wavelet software was provided by C. Torrence and G. Compo, and is available at http://paos.colorado.edu/research/wavelets/.

REFERENCES

Anfinogentov, S., Nakariakov, V. M., Mathioudakis, M., Van Doorsselaere, T., & Kowalski, A. F. 2013, ApJ, 773, 156
Asai, A., Kiyohara, J., Takasaki, H., Narukage, N., Yokoyama, T., Masuda, S., Shimojo, M., & Nakajima, H. 2013, ApJ, 763, 87
Aschwanden, M. J. 2004, Physics of the Solar Corona. An Introduction (Praxis Publishing Ltd)
Aschwanden, M. J., & Benz, A. O. 1997, ApJ, 480, 825
Balona, L. A., Broomhall, A.-M., Kosovichev, A., Nakariakov, V. M., Pugh, C. E., & Van Doorsselaere, T. 2015, MNRAS, 450, 956
Bárta, M., Karlický, M., Vršnak, B., & Goossens, M. 2007, Central European Astrophysical Bulletin, 31, 165
Bárta, M., Vršnak, B., & Karlický, M. 2008, A&A, 477, 649
Bastian, T. S., Benz, A. O., & Gary, D. E. 1998, ARA&A, 36, 131
Botha, G. J. J., Arber, T. D., Nakariakov, V. M., & Zhugzhda, Y. D. 2011, ApJ, 728, 84
Brueckner, G. E., et al. 1995, Sol. Phys., 162, 357
Chen, P. F., & Priest, E. R. 2006, Sol. Phys., 238, 313
Cheung, M. C. M., et al. 2015, ApJ, 801, 83
de Moortel, I. 2009, Space Sci. Rev., 149, 65
De Moortel, I., & Nakariakov, V. M. 2012, Royal Society of London Philosophical Transactions Series A, 370, 3193
Doyle, J. G., Popescu, M. D., & Taroyan, Y. 2006, A&A, 446, 327
Fan, Y. 2009, ApJ, 697, 1529
Fárník, F., Karlický, M., & Švestka, Z. 2003, Sol. Phys., 218, 183
Fletcher, L., & Hudson, H. S. 2008, ApJ, 675, 1645
Golub, L., et al. 2007, Sol. Phys., 243, 63
Gosling, J. T., Teh, W.-L., & Eriksson, S. 2010, ApJ, 719, L36
Horne, J. H., & Baliunas, S. L. 1986, ApJ, 302, 757
Howard, R. A., et al. 2008, Space Sci. Rev., 136, 67
Hudson, H. S. 2000, ApJ, 531, L75
Hurford, G. J., et al. 2002, Sol. Phys., 210, 61
Kai, K. 1986, Sol. Phys., 104, 235
Karlický, M., Bárta, M., & Rybák, J. 2010, A&A, 514, A28
Kliem, B., Karlický, M., & Benz, A. O. 2000, A&A, 360, 715
Kumar, P., & Cho, K.-S. 2013, A&A, 557, A115
Kumar, P., & Cho, K.-S. 2014, A&A, 572, A83
Kumar, P., Cho, K.-S., Bong, S.-C., Park, S.-H., & Kim, Y. H. 2012, ApJ, 746, 67
Kumar, P., Innes, D. E., & Inhester, B. 2013, ApJ, 779, L7
Kumar, P., & Manoharan, P. K. 2013, A&A, 553, A109
Kumar, P., Nakariakov, V. M., & Cho, K.-S. 2015, ApJ, 804, 4
Kumar, P., Srivastava, A. K., Somov, B. V., Manoharan, P. K., Erdélyi, R., & Uddin, W. 2010, ApJ, 723, 1651
Kundu, M. R. 1961, J. Geophys. Res., 66, 4308
Kundu, M. R. 1965, Solar radio astronomy
Kundu, M. R., White, S. M., Gopalswamy, N., & Lim, J. 1994, ApJS, 90, 599
Lee, E. J., Archontis, V., & Hood, A. W. 2015, ApJ, 798, L10
Lemen, J. R., et al. 2012, Sol. Phys., 275, 17
Lin, R. P., et al. 2002, Sol. Phys., 210, 3
Liu, W., & Ofman, L. 2014, Sol. Phys., 289, 3233
Liu, W., Ofman, L., Nitta, N. V., Aschwanden, M. J., Schrijver, C. J., Title, A. M., & Tarbell, T. D. 2012, ApJ, 753, 52
Longcope, D. W., & Welsch, B. T. 2000, ApJ, 545, 1089
Masson, S., Pariat, E., Aulanier, G., & Schrijver, C. J. 2009, ApJ, 700, 559
Mathioudakis, M., Seiradakis, J. H., Williams, D. R., Avgoloupis, S., Bloomfield, D. S., & McAteer, R. T. J. 2003, A&A, 403, 1101
Metcalf, T. R., Hudson, H. S., Kosugi, T., Puetter, R. C., & Pina, R. K. 1996, ApJ, 466, 585
Moore, R. L., Sterling, A. C., & Falconer, D. A. 2015, ApJ, 806, 11
Nakajima, H., et al. 1994, IEEE Proceedings, 82, 705
Nakajima, H., Sekiguchi, H., Sawa, M., Kai, K., & Kawashima, S. 1985, PASJ, 37, 163
Nakariakov, V. M., Foullon, C., Verwichte, E., & Young, N. P. 2006, A&A, 452, 343
Nakariakov, V. M., Inglis, A. R., Zimovets, I. V., Foullon, C., Verwichte, E., Sych, R., & Myagkova, I. N. 2010, Plasma Physics and Controlled Fusion, 52, 124009
Nakariakov, V. M., & Melnikov, V. F. 2009, Space Sci. Rev., 149, 119
Nakariakov, V. M., & Zimovets, I. V. 2011, ApJ, 730, L27
Ning, Z., Innes, D. E., & Solanki, S. K. 2004, A&A, 419, 1141
Pandey, J. C., & Srivastava, A. K. 2009, ApJ, 697, L153
Pariat, E., Antiochos, S. K., & DeVore, C. R. 2010, ApJ, 714, 1762
Pascoe, D. J., Nakariakov, V. M., & Kupriyanova, E. G. 2013, A&A, 560, A97
Pesnell, W. D., Thompson, B. J., & Chamberlin, P. C. 2012, Sol. Phys., 275, 3
Pontin, D. I., Priest, E. R., & Galsgaard, K. 2013, ApJ, 774, 154
Pugh, C. E., Nakariakov, V. M., & Broomhall, A.-M. 2015, ApJ, 813, L5
Roberts, B. 2000, Sol. Phys., 193, 139
Scargle, J. D. 1982, ApJ, 263, 835
Schou, J., et al. 2012, Sol. Phys., 275, 229
Sych, R., Nakariakov, V. M., Karlicky, M., & Anfinogentov, S. 2009, A&A, 505, 791
Tajima, T., Sakai, J., Nakajima, H., Kosugi, T., Brunel, F., & Kundu, M. R. 1987, ApJ, 321, 1031
Takasao, S., Asai, A., Isobe, H., & Shibata, K. 2012, ApJ, 745, L6
Takasao, S., Matsumoto, T., Nakamura, N., & Shibata, K. 2015, ApJ, 805, 135
Torrence, C., & Compo, G. P. 1998, Bulletin of the American Meteorological Society, 79, 61
Tsuneta, S., et al. 2008, Sol. Phys., 249, 167
Wang, H., & Liu, C. 2012, ApJ, 760, 101
White, S. M., Krucker, S., Shibasaki, K., Yokoyama, T., Shimojo, M., & Kundu, M. R. 2003, ApJ, 595, L111
Wuelser, J.-P., et al. 2004, in Society of Photo-Optical Instrumentation Engineers (SPIE) Conference Series, Vol. 5171, Telescopes and Instrumentation for Solar Astrophysics, ed. S. Fineschi & M. A. Gummin, 111
Yashiro, S., Gopalswamy, N., Michalek, G., St. Cyr, O. C., Plunkett, S. P., Rich, N. B., & Howard, R. A. 2004, Journal of Geophysical Research (Space Physics), 109, 7105